Non-Invasive On-Chip Light Observation by Contactless Waveguide Conductivity Monitoring

Francesco Morichetti, Stefano Grillanda, Marco Carminati, *Member, IEEE*, Giorgio Ferrari, *Member, IEEE*, Marco Sampietro, Michael J. Strain, Marc Sorel, and Andrea Melloni

I. Introduction

EVOLUTION from single device level to complex systems on-a-chip is envisioned as a fundamental step to fully exploit the potential of photonic integration [1]. Even though photonic platforms are ready to miniaturize several thousands of elements on a single chip [2], one of the main barriers to the development of large scale integration is the lack of non-invasive monitoring tools to inspect the light inside optical waveguides. Circuit monitoring and feedback control operations are required to counteract fabrication tolerances, environmental fluctuations, and mutual crosstalk effects [3], [4], especially when many photonic devices are aggregated into complex circuits. To this aim, the current status of each part of the circuit needs to be inspected real-time without altering its working point. As long as the components count in a circuit is limited to a few units, light monitoring can be achieved by tapping a small fraction of the optical power from the waveguide and rerouting it to a photodetector [5], [6]. Yet, when hundreds or thousands of devices are integrated, the number of probing points increases accordingly, and any light attenuation or perturbation should be avoided [7].

Light tapping from the waveguide can be circumvented by using the waveguide itself as a power monitor. In silicon waveguides, where material absorption is inhibited at wavelengths above 1.1 μm, photocarrier generation has been demonstrated by exploiting two photon absorption (TPA) [8], [9], and sub-bandgap absorption mechanisms, including surface-state absorption (SSA) [10], [11] and defect mediated absorption induced via selective ion-implantation [12], [13]. However, power monitors proposed so far based on these effects require the waveguide core to be electrically contacted through highly doped regions [11]–[13] or electric lines [10] to sweep out carriers from the absorbing region. This leads to additional optical loss that limits the number of probing points to a few units. The development of minimally-invasive waveguide power monitors still presents one of the key challenges for integrated optical technology [7].

Here, we demonstrate non-invasive light observation in silicon photonics devices by exploiting photon interaction with intra-gap energy states localized at the waveguide surface. The physical effect exploited in our technique is the change of the waveguide conductance induced by native interaction of photons with the intra-gap energy states localized at the Si-SiO_2 interface [14] that exist even in an ideal roughness-free interface [15]. Unlike other techniques, a capacitive access to the waveguide is used, thereby avoiding direct contact with the waveguide core, and no specific treatments at the waveguide surface need to be done. Neither photon tapping is required nor appreciable perturbation on the optical field is introduced, thereby implementing a truly non-invasive light observation.

The paper is organized as follows. Section II introduces the concept of the CLIPP and the fabrication process required to realize the device. Experimental results are presented in Section III, showing the performance of the CLIPP in the monitoring of the light in silicon waveguides and microring resonators, as well as its application to multipoint circuit probing.

Manuscript received December 10, 2013; accepted January 9, 2014. This work was supported by the Italian PRIN 2009 project Shared Access Platform to Photonic Integrated Resources (SAPPHIRE), by Fondazione Cariplo (Grant no. 2011-2118), and by the European Project BBOI of the 7th EU Framework Program.

F. Morichetti, S. Grillanda, M. Carminati, G. Ferrari, M. Sampietro, and A. Melloni are with the Dipartimento di Elettronica, Informazione e Bioingegne-ria, Politecnico di Milano, 20133 Milano, Italy (e-mail: francesco.morichetti@ polimi.it; grillanda@elet.polimi.it; marco1.carminati@polimi.it; giorgio. ferrari@polimi.it; marco.sampietro@polimi.it; melloni@elet.polimi.it).

M. J. Strain is with the Institute of Photonics, The University of Strathclyde, Glasgow G4 0NW (e-mail: Michael.strain@strath.ac.uk).

M. Sorel is with the School of Engineering University of Glasgow, Glasgow, G12 8QQ, U.K. (e-mail: Marc.Sorel@glasgow.ac.uk).

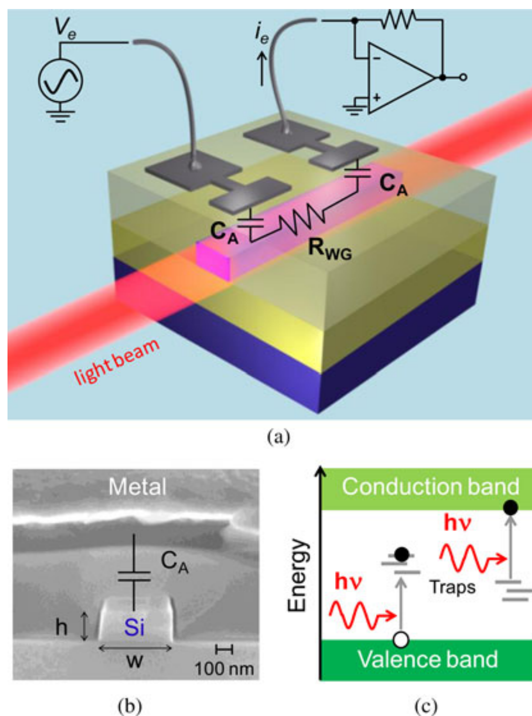

Fig. 1. Non-invasive light observer integrated on a silicon chip. (a) Illustration of the CLIPP device consisting of two metal electrodes deposited onto the electrically-insulating upper cladding and capacitively coupled (C_A) to the electrically-resistive (R_{WG}) silicon nanowaveguide. (b) SEM photograph of the silicon waveguide cross section. (c) Sketch of two possible alternative SSA mechanisms where intra-gap energy states create a free carrier and a corresponding recombination center.

The non-invasive nature of the CLIPP is experimentally demonstrated in Section IV. In Section V the use of the CLIPP in the tuning of photonic integrated circuits is shown. Details on the electric system employed for the read-out of the waveguide impedance are provided in Section VI. A concluding section summarizes the main results and discusses potential application fields of the CLIPP. In the Appendix, an in-depth analysis on the physical mechanisms affecting the electric conductance of silicon waveguides is reported.

II. The CLIPP Device

A. Concept

The concept of the CLIPP is schematically shown in Fig. 1(a). The CLIPP simply consists of two electrodes surrounding the optical waveguide and spaced from the silicon core by an electrically insulating layer. In the configuration of Fig. 1(a), both electrodes are located above the waveguide on top of the upper cladding layer. A silicon channel waveguide with a rectangular core region is here considered, but the CLIPP can be potentially applied to arbitrary waveguide geometries, such as shallow and deep etched rib waveguides, slot waveguides, or photonic crystal waveguides.

To explain the working principle of the CLIPP, let us consider the behavior of the silicon waveguide in the electric domain. Because of the typical doping level of commercial SOI wafers (10^{15} cm^{-3}, p-type), the silicon core acts as a conductive wire, whose resistance $R_{WG} = \sigma^{-1} L/wh$ depends on the width w and the height h of the Si core, on the length L of the considered waveguide section (i.e. the distance between the two electrodes), and on the electrical conductivity σ of silicon. The latter is related to the average number of free carriers locally contained in the silicon material. For instance, in the waveguide of Fig. 1(b) ($w = 480$ and $h = 220$ nm) about 10^2 free holes are expected to be distributed in the volume of a 1-μm-long waveguide section, thus providing a conductance of about 8 nS for a 100 μm-long waveguide.

As the light propagates in the waveguide, additional free carriers are generated by SSA mechanisms [see Fig. 1(c)], that locally modify the waveguide conductivity, and hence the overall electric conductance $G = 1/R_{WG}$ (details on the physical phenomena affecting the electric conductance of silicon waveguides are reported in the Appendix). Therefore, a measurement of the light dependent change of the waveguide conductance ΔG provides information on the light intensity in the waveguide.

In order to implement a truly non-invasive light observation, the CLIPP exploits a capacitive access to the waveguide, thereby avoiding direct contact with the waveguide core. For the channel waveguide of Fig. 1(b), the electrodes are spaced from the silicon core by a 1-μm-thick silica film, providing the access capacitance C_A to the waveguide. At the wavelength of 1550 nm, the optical intensity at the SiO_2-metal interface is 80 dB below its peak value in the waveguide, so that the electrodes do not induce any detectable change in the waveguide propagation loss, amounting to 2 dB/cm.

Neglecting parasitic effects due to the Si substrate and to the capacitance between the electrodes, that are discussed in details in SectionVI, the equivalent electric circuit of the CLIPP simply consists of two access capacitances C_A in series with the waveguide resistance R_{WG}. The light dependent conductance variation ΔG can be thus inferred from the measurement of the overall electric impedance at the two metal electrodes through an ultra sensitive impedance measurement system. The experimental setup used in this study is described in Section III-A [16].

B. Technology and Fabrication

The silicon waveguides are fabricated on a commercial silicon-on-insulator (SOI) wafer with a 220-nm thick silicon core on a 2-μm thick oxide buffer layer. The waveguide pattern is written on a hydrogen silsesquioxane (HSQ) resist through electron-beam lithography and then transferred to the silicon core by an inductively coupled plasma etching process [17]. A residual 80-nm thick HSQ cap layer on top of the waveguide is visible in the SEM picture of Fig. 1(b). The waveguide core is buried under a 1-μm thick cover layer, consisting of 550 nm of spun and baked HSQ and 450 nm of silicon dioxide grown by plasma enhanced chemical vapor deposition (PECVD).

The electrodes of the CLIPP consist of a 200 nm thick Au film deposited onto the silica cladding (with an intermediate 20 nm thick Ti adhesion layer) and patterned by a lift-off technique. The CLIPP can be fabricated by using any CMOS compatible metal technology and can exploit conventional processes used for realizing thermal actuators, without additional process steps [18].

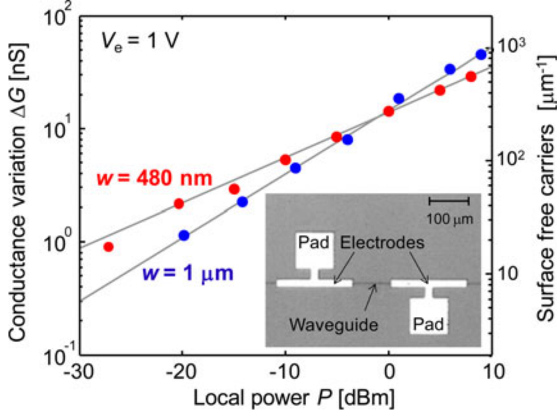

Fig. 2. Optical power monitoring performed with a CLIPP. Measured conductance variation ΔG versus the optical power P for a single mode ($w = 480$ nm, red circles) and a multimode ($w = 1$ μm, blue circles) silicon waveguide. The CLIPP is driven at $V_e = 1$ V and $f_e = 1$ MHz, metal electrodes (20 μm $\times$ 200 μm) are placed at distance $L = 100$ μm. The 100 μm $\times$ 100 μm metal pads are used for wire bonding with the impedance read-out system.

Inversely tapered waveguide sections, buried in a SU-8 polymer waveguide, were realized at the chip's facets in order to reduce coupling loss with optical lensed fibers (1.7 μm mode field diameter) to 5 dB/facet.

III. Experimental Results

A. Experimental Setup

The real and imaginary parts of the waveguide impedance are measured through a synchronous detection architecture, including a low-noise transimpedance amplifier (model DHPCA-100 by Femto) coupled to a high precision lock-in demodulator (HF2LI by Zurich Instruments). In order to measure ΔG, a sinusoidal voltage V_e at a frequency f_e is applied to one electrode of the CLIPP, the other being connected to a transimpedance amplifier to sense the flowing current i_e. The transimpedance amplifier has a 10^4 V/A conversion gain, a bandwidth of 80 MHz and a 6 pA/$\sqrt{\text{Hz}}$ minimum noise floor at 1 Hz integration bandwidth, resulting in a total measured rms noise of $\sim$80 pS. In the perturbation measurement discussed in Section IV, the output optical signal is detected by an external photodiode and sent to a second channel of the lock-in detector, enabling synchronous detection of the optical and the electrical signals.

The temperature of the optical chip is controlled within 0.1 K by a Peltier thermocooler integrated inside a customized holder. The state of polarization of the input light is controlled with a polarization controller providing an extinction ratio greater than 30 dB between the excited quasi-transverse electric (TE) and quasi-transverse magnetic (TM) modes over a wavelength range of 20 nm around 1550 nm. In all the measurements presented in this study the light signal is TE polarized.

B. Light Induced Conductance Change

The measured conductance variation ΔG versus the optical power P is shown in Fig. 2 for a single mode ($w = 480$ nm, red circles) and a multimode ($w = 1$ μm, blue circles) silicon waveguide. Light intensity was observed over a dynamic range of 4 orders of magnitude, down to -30 dBm (1 μW), this performance largely fulfilling the requirements of several practical applications. A response time down to 50 μs was achieved by driving the device with a voltage $V_e = 1$ V and a frequency $f_e =$ 1 MHz. The inset shows a top-view photograph of the device with a 100-μm-long waveguide section enclosed between two narrow electrodes.

An in-depth analysis was carried out to identify SSA as the physical effect responsible for the change of waveguide conductance ΔG. Results show that ΔG is associated with a carrier density variation rather than with a carrier mobility variation, and that TPA–mediated photocarrier generation is negligible (see Appendix). The sensitivity of the CLIPP is related to the density of free carriers generated by SSA, that depends on the intensity of the optical mode on the waveguide boundaries [10], where surface states are located (typically within the first three/four silicon atomic layers [19]).

For the waveguides considered in Fig. 2, the integral intensity of the light along the waveguide perimeter is similar, resulting in a comparable conductance variation ΔG for the same power P of the guided mode. This small geometrical sensitivity enables application of the technique without imposing specific constraints to the design of the optical waveguide. A comparable sensitivity on TM polarization was also observed. To improve the CLIPP sensitivity, the modal overlap with the surface can be increased by suitably engineering the cross-sectional waveguide geometry [10], yet at the price of a higher propagation loss [20].

The slope of the log-log ΔG-P curves is related to the density of carriers generated at the surface. A sub-linear relationship is observed, that is consistent with a situation in which the number of photo-generated carriers is larger than those thermally available. A similar behaviour has been reported also in metal oxide semiconductor (MOS) devices [21] and in high gap conductors [22]. In this regime an increase of the optical power results not only in a larger carrier density but also in a reduction of their recombination time [23]. This condition is verified in both devices of Fig. 2, where, at $P = -10$ dBm ($\Delta G \approx 5$ nS), about 10^2 μm^{-1} free carriers are locally photogenerated at the surface of a 1-μm-long waveguide section, this number being comparable with the density of native free holes distributed across the waveguide in absence of light. For the same value of optical power P, the single mode waveguide (shorter perimeter) has a higher carrier density with respect to the multi-mode waveguide (larger perimeter), resulting in a slightly lower recombination time, and consequently in a small reduction of the ΔG-P exponent.

The density of free carriers generated by SSA per unit length (Fig. 2, right vertical axis) is estimated by assuming that the photogeneration is homogeneous along the waveguide with a density of photogenerated holes equals to the density of photogenerated electrons, $\Delta N_{e,s} = \Delta N_{h,s} = \Delta N_s/2$. Further, the mobility of carriers generated at the surface ($\mu_{e,s} = 500$ cm^2/V$\cdot$s and $\mu_{h,s} = 150$ cm^2/V$\cdot$s) is about 30% [24] of the free carriers mobility in the bulk. Thus we obtain:

$$\Delta G = \Delta\sigma \frac{A}{L} = q\left(\frac{\mu_{e,s} + \mu_{h,s}}{2}\right)\frac{A}{L}\Delta N_s \qquad (1)$$

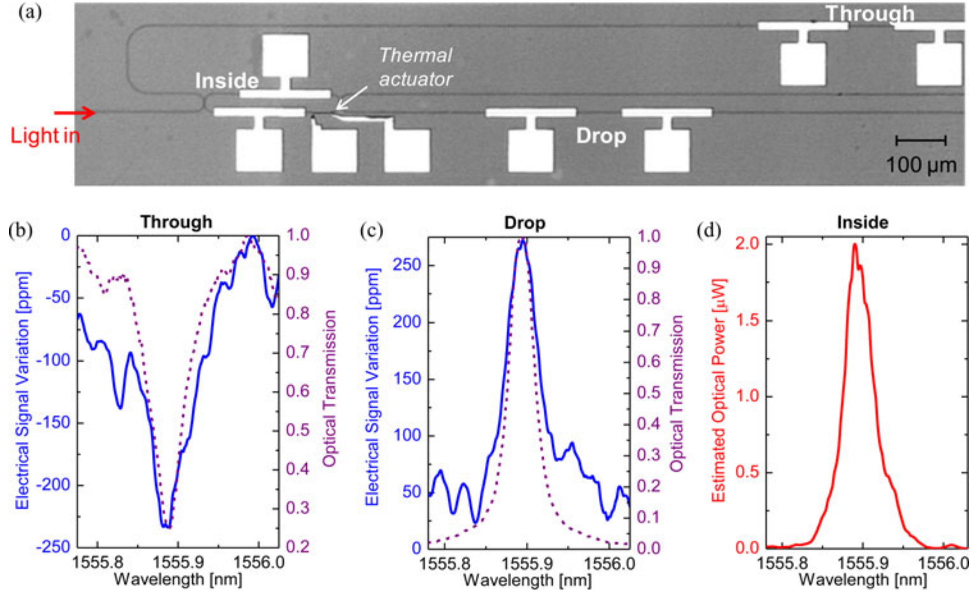

Fig. 3. Non-invasive monitoring of a silicon photonic integrated circuit. (a) Top-view optical microscope photograph of a racetrack microresonator with a CLIPP at both the Through and the Drop port bus waveguides, and with an inner CLIPP inside the resonator. The resonator has a radius of 20 μm and a geometric length of 644 μm. (b) Through and (c) Drop port TE transmission measured with an external OSA (purple dashed curves) and with the on-chip CLIPPs (blue solid curves). The amplitude and the frequency of the electric signal driving the CLIPPs are $V_e = 1$ V and $f_e = 2$ MHz, respectively. (d) The intracavity optical power around the resonant wavelength is retrieved from the electric signal of the CLIPP inside the resonator.

from which the value of the linear density of surface free carriers (ΔN_s) plotted in Fig. 2 is calculated.

C. Multipoint Light Monitoring

Many light monitors can be placed in strategic positions around the chip enabling real time management of complex integrated optical systems. We fabricated a racetrack silicon resonator [see Fig. 3(a)] equipped with three CLIPPs: one inside the resonator and the other two at the Through and Drop ports respectively. The same metal technology of the CLIPP is used to realize a thermo-optic actuator inside the resonator for the feedback control of its resonant wavelength [18].

To set a benchmark for performance evaluation, the CLIPPs were first switched OFF ($V_e = 0$) and the reference transmission spectra of the resonator were measured through a tunable laser with 1 pm resolution, synchronized with an optical spectrum analyzer (OSA). Fig. 3(b)–(c) shows in purple dashed lines the transmission of the resonator at the Through and Drop ports, respectively. The measured 3 dB linewidth and free spectral range (FSR) are 36 pm and 860 pm, respectively, resulting in a Q factor of about 43 000. Measurements were repeated with the three CLIPPs switched on at V_e up to 10 V, and no detectable changes of the resonator spectrum and of the intrinsic Q factor (about 55000) were observed.

The transmission spectra of the resonator were then measured by using the CLIPPs integrated at the Through [Fig. 3(b), blue solid line] and at the Drop [Fig. 3(c), blue solid line] ports. The electric signal of the CLIPP provides a direct measurement of the resonance wavelength of the resonator, with less than 1 pm shift compared to the OSA reference. By using the calibration curve of Fig. 2, we also retrieved the spectral line and the optical power level inside the resonator, as shown in Fig. 3(d). The 3 dB linewidth, measured at a power level of -30 dBm, is less than 2 pm larger than the OSA measurement, thus demonstrating the accuracy of the CLIPP.

IV. Perturbation Analysis

The non-invasive nature of the CLIPP was explored by looking for the existence of a signal component at the read-out frequency f_e in the output optical signal with a highly sensitive lock-in based detection system (details in Section VI).

As no evidence of disturbance was detected on bare waveguides, we investigated the perturbative effects on high-Q optical microresonators. We injected a continuous-wave (CW) light into the resonator of Fig. 3(a) and measured the ratio between the power $P(f_e)$ at $f_e = 2$ MHz and the average power P_{CW} of the optical signal outgoing from the Through port, this ratio being typically referred to as modulation index of an intensity modulated signal. The inner CLIPP was driven at $V_e = 1$ V and the wavelength scanned across 0.2 nm around the resonant wavelength $\lambda_r = 1555.889$ nm. As shown in Fig. 4(a) (purple line), the modulation index $P(f_e)/P_{CW}$ is minimum at λ_r, where the slope of the transmission spectrum of the resonator (green line) vanishes, whereas it exhibits local maxima at $\lambda_p = \lambda_r \pm 9$ pm, where the slope of the spectrum is maximum. This result provides clear evidence that the perturbation is due to a refractive index modulation effect, causing a tiny wavelength shift of the resonator spectrum and an intensity modulation of the output signal [25].

The relative perturbation at the frequency f_e of the electric signal driving the CLIPP can be expressed as

$$\frac{P(f_e)}{P_{CW}} = \frac{1}{H}\frac{\partial H}{\partial \lambda}d\lambda = \lambda_r \frac{1}{H}\frac{\partial H}{\partial \lambda}\frac{dn_{\text{eff}}}{n_g}\frac{L_e}{L_r} \tag{2}$$

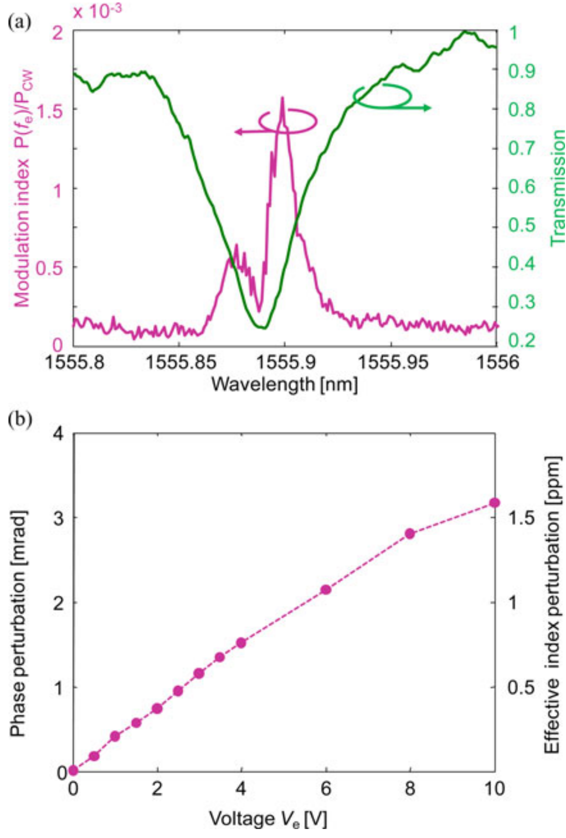

Fig. 4. Analysis of the perturbative effects induced by the CLIPP. (a) The purple curve shows the ratio between the perturbation $P(f_e)$, given by the power of the optical signal modulated at the frequency of the electric signal, and the power of the optical signal P_{CW}. The measurement is carried out on the optical signal outgoing from the Through port of the resonator of Fig. 3. The asymmetry in the measured perturbation is inherently associated to the non-symmetric transmission spectrum of the resonator (green curve). (b) Phase perturbation and effective index perturbation induced by the CLIPP. Typical driving voltage of the CLIPP is about 1 V.

where H is the intensity transmission spectrum of the ring resonator at the Through port, $d\lambda$ is the shift of the resonant wavelength λ_r due to the induced perturbation dn_{eff} of the waveguide effective index, and n_g is the waveguide effective group index. The ratio L_e/L_r takes into account that the index perturbation does not occur along the entire ring length L_r, but only in a portion of length L_e underneath the metal electrode where the voltage V_e is applied. For the device of Fig. 3(a) driven at a voltage $V_e = 1$ V, we measured a maximum relative perturbation $P(f_e)/P_{CW} = 1.65 \cdot 10^{-3}$ (-27.8 dB) at the wavelength $\lambda_p = 1555.898$ nm (where $\partial H/\partial\lambda = 30$ nm^{-1}) corresponding to a resonance shift $d\lambda = 55$ fm (6.8 MHz), that is less than 0.1% of the resonator linewidth.

This tiny perturbation is really negligible in most applications. For instance, assuming that a resonant shift of less than 10% of the resonator linewidth is acceptable, then the CLIPP can be used to monitor resonators with a bandwidth as narrow as 50 MHz, that is with a Q factor of about $4 \cdot 10^6$. Hence, the CLIPP can be applied without any disturbance to the silicon microring resonators with the highest Q factor realized so far [26], which is in the order of $7.6 \cdot 10^5$.

Furthermore, by substituting in eq. (2) the values of the geometric ($L_e = 200$ μm, $L_r = 644$ μm) and optical ($n_g = 4.22$) parameters of the considered structure, we derived an effective index perturbation $dn_{\mathrm{eff}} = 5 \cdot 10^{-7}$, amounting to about 0.2 ppm of the waveguide effective index $n_{\mathrm{eff}} = 2.45$, and corresponding to a phase modulation induced of $d\phi = 2\pi dn_{\mathrm{eff}} L_e/\lambda_p = 0.4$ mrad. Also, if assuming a thermo-optic coefficient of $1.84 \cdot 10^{-3}$ K^{-1} for the silicon waveguide [27], the induced perturbation is comparable to that induced by a temperature change of 2.7 mK, which is about two orders of magnitude below the thermal stability limit guaranteed by conventional thermo electric coolers and can be considered negligible in practical applications.

Finally, we investigated the physical mechanism originating such a tiny perturbation, by exploring the behavior of the CLIPP up to an applied voltage of $V_e = 10$ V. As shown in Fig. 4(b), the linearity of the measured perturbation versus V_e rules out the existence of a significant thermal heating of the waveguide due to a current flow along the silicon core, which would rather exhibit a quadratic behavior versus V_e. Results are instead consistent with a linear electro-optic Pockels effect, according to which the refractive index variation dn of the silicon core is related to the applied electric field E by

$$dn = \frac{n^3}{2} r E = \frac{\chi^{(2)}}{n} E \tag{3}$$

where $\chi^{(2)}$ is the second-order susceptibility. In our experiment, the change of the waveguide effective index dn_{eff} corresponds to $dn = 7 \cdot 10^{-7}$ (at $V_e = 1$ V) and the average electric field in the 3-μm-thick silica layer underneath the electrode is $E = 0.3$ V/μm. These values lead to an electro-optic coefficient $r = 0.1$ pm/V ($\chi^{(2)} = 5$ pm/V) that is consistent with other reports of non-intentionally strained silicon waveguides [28].

V. Tuning of Photonic Integrated Circuits

The usefulness of the CLIPP to control and tune the transfer function of a photonic integrated circuit was demonstrated on a circuit composed of two directly coupled racetrack resonators. Fig. 5(a) shows a top-view microphotograph of the fabricated device. The two resonators have the same geometric length $L_r = 644$ μm, resulting in a FSR of about 860 pm. The power coupling coefficient between the resonators is 0.05, while the coupling between the bus waveguides and the rings is 0.1. Thermal actuators are placed on the waveguide of each resonator to independently tune their resonances. CLIPPs are positioned on the Through port and inside each resonator to monitor the light power in each relevant portion of the circuit.

In order to show the accuracy of the CLIPP monitoring approach, the electric signal $\Delta G/G$ measured by the CLIPP located at the Through port of the circuit [Fig. 5(b)] is directly compared to the optical signal acquired at the same output port by using an OSA [Fig. 5(c)]. The two signals were simultaneously acquired for several tuning configuration of the device. In Fig. 5(b)–(c), green dashed lines show the transmission spectrum when thermal actuators are switched off (0 V). Even though the two resonators are nominally identical, due to fabrication tolerances

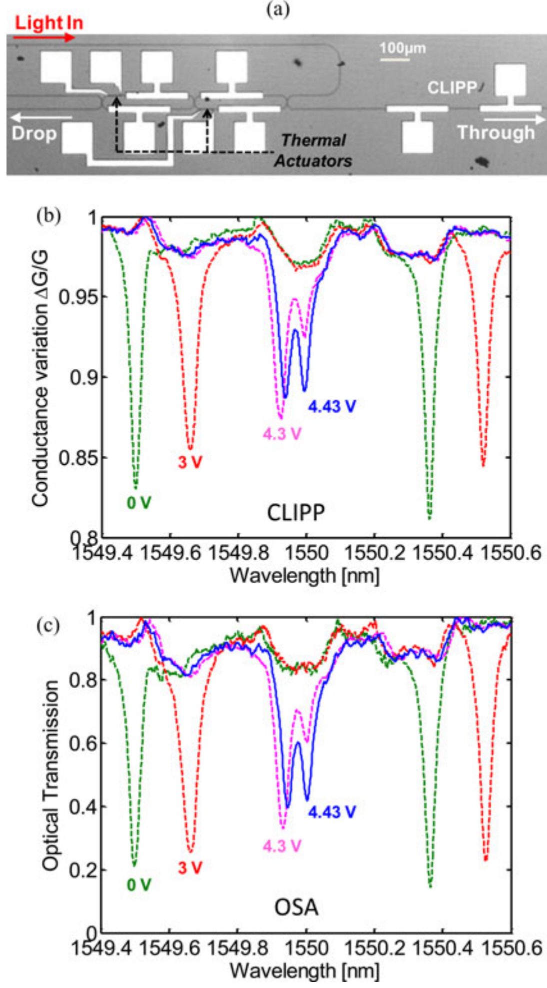

Fig. 5. (a) Layout of the two-ring filter with CLIPPs placed at the Through port and inside the ring resonators, and with thermal actuators enabling to adjust the resonance of each ring. (b) Normalized conductance $\Delta G/G$ measured by the CLIPP ($V_e = 1$ V, $f_e = 2$ MHz) placed at the Through port for different voltage applied by the thermal actuator. (c) Optical transmission measured at the Through port by a conventional OSA for different voltage applied to the thermal actuator.

the two resonant frequencies are shifted by about half FSR, the resonance of the first resonator (the one coupled to the input bus waveguide) being around 1549.45 nm, while the resonance of the second resonator being around 1550 nm. Starting from this condition, the heater placed on the first resonator is switched on to align the resonant frequency to that of the other resonator. When the voltage is increased from 0 V to 4.43 V, the resonance mismatch is thermally compensated and the two ring resonances overlap (blue solid lines). An excellent agreement is found between the CLIPP response and OSA reference spectrum for any tuning condition of the device.

This result demonstrates that the CLIPP can be effectively used to monitor the working point of a generic photonic integrated circuit, regardless of the presence of other cascaded devices. Information on individual device operation reduces the complexity of tuning algorithms, that would become prohibitive when a large number of devices are integrated in a complex architecture. A systematic investigation of the frequency response

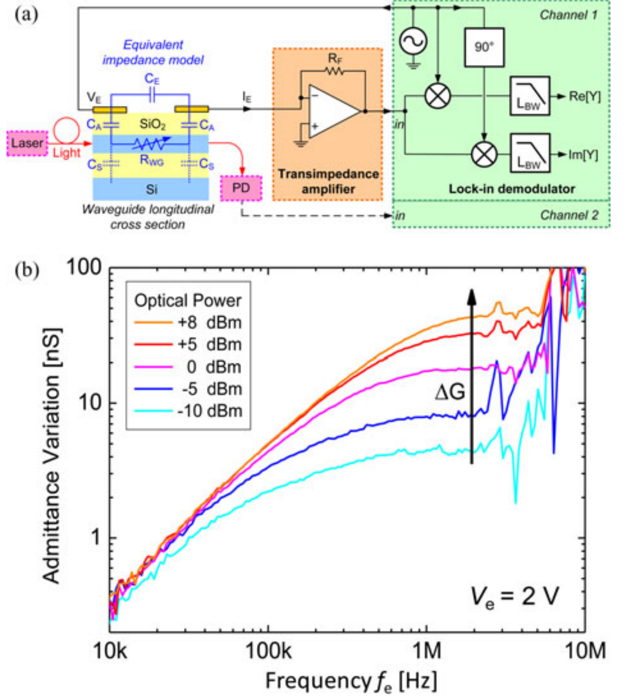

Fig. 6. (a) Scheme of the electric impedance read-out system, consisting of a low-noise transimpedance amplifier (with feedback resistance R_F) combined with a precision lock-in detector with bandwidth L_{BW}. The equivalent impedance model of the CLIPP is also shown. (b) Measured differential admittance spectra (with respect to the absence of light) for increasing optical power levels.

of the CLIPP will be carried out in future works, in order to assess its performance in feedback-controlled automatic tuning systems.

VI. Electric Impedance Read-Out System

In this section, further details are provided on the electric model of the CLIPP, on the read-out system employed for the measurement of the electric impedance, and on the optimization of the CLIPP design.

Fig. 6(a) shows a scheme of the read-out system and the electric equivalent model of the CLIPP. The access capacitance C_A to the waveguide can be estimated (neglecting fringing field effects) as a parallel plate capacitor $C_A = \varepsilon_0 \varepsilon_{ox} w L_e / t_{ox}$, where t_{ox} and ε_{ox} are the thickness and relative dielectric constant of the SiO_2 upper cladding layer, respectively, and ε_0 is the vacuum permittivity. Similarly, the nominal value of the waveguide resistance in absence of light is $R_{WG} = \sigma^{-1} L/wh$ where σ^{-1} $\sim$1 MΩ/μm is the bulk resistivity of the waveguide. In parallel to the main C_A-R_{WG} path, a parasitic capacitance C_E is generated by the stray coupling between the electrodes (measured in the 0.16 – 0.8 pF range depending on the geometry of the CLIPP electrodes and on the connection wires arrangement). Since in the MHz range the impedance associated to C_E is about 3 orders of magnitude smaller than that of R_{WG}, a lock-in system with 100 ppm resolution is required.

Fig. 6(b) shows the variation of the absolute value of the admittance Y measured at the CLIPP electrodes. The change

of waveguide conductance ΔG can be extracted by subtracting the reference spectrum of the waveguide admittance (measured in absence of light) from the admittance spectra measured at different optical power levels P. The increase of the plateau level (around 1 MHz in the figure) provides information on ΔG. The spectral position of this plateau is set by the frequency $f_A = 1/(2\pi C_A/2R_{WG})$ of the pole associated with C_A.

Once w, h, and t_{ox} are fixed according to waveguide optimization criteria, the frequency f_A of the CLIPP can be conveniently adjusted by a suitable choice of the electrodes distance L and of the electrode length L_e. In our case, where $L = 100\ \mu$m ($C_A \sim 5$ fF) and $L_e = 200\ \mu$m, the resulting f_A is about 1 MHz.

Miniaturization of the CLIPP is possible, yet at the price of a higher f_e, since f_A shifts at higher frequencies when L or L_e are reduced. However, a physical upper limit to f_e is set also by the presence of the stray capacitances C_S between the waveguide core and the silicon substrate through the bottom oxide. In fact, this distributed capacitance attenuates the applied electrical signal due to the high frequency partition between C_A and C_S.

In principle, the operative frequency f_e depends also on the thickness t_{ox} of the upper cladding oxide. However, standard deposition techniques guarantee a control of better than 10 nm in the film thickness. This small tolerance introduces no significant variability in the CLIPP performance, because it only induces a 1% change of f_A and thus of f_e.

VII. Conclusion

We have reported on a non-invasive on-chip light observer enabling the monitoring of the optical intensity in silicon waveguides without introducing any significant perturbation. The CLIPP exploits a contactless capacitive access to the waveguide, featuring a size of a few hundreds of microns, −30 dBm sensitivity and dynamic range of 40 dB. Thanks to its non-invasive nature, the CLIPP can be integrated into generic photonic devices, including high-Q resonators. It also enables the monitoring of individual devices embedded inside arbitrary complex architectures, thereby reducing the complexity of feedback control algorithms that would become otherwise prohibitive when a high number of components are integrated. Scalability to a large number of probing points per chip is conceivable thanks the CLIPP compactness and manufacturing simplicity.

Compatibility with complementary metal oxide (CMOS) production lines opens to direct integration of the electronic circuits into the same photonic chip, enabling read-out and processing through lock-in architectures with hundreds of amplifiers and mixers [29]. These considerations provide a viable way to make photonics break away from today's device level up to a system-on-chip level [1], so as to fulfil the requirements of wide-ranging application fields, such as telecom [30], optical interconnects [31], biosensing [32], quantum manipulation and computing [33]–[35], and chip-to-chip quantum communications [36]. Furthermore, the possibility of applying a CLIPP at any point across a photonic wafer makes it a powerful tool for wafer scale automated testing, without requiring expensive bulk optical measurement rigs.

Appendix

In this Appendix, the physical mechanisms affecting the electric conductance of silicon waveguides are carefully investigated. Here, we identify SSA as the only physical effect responsible for the change of waveguide conductance ΔG versus the local optical power P (as shown in Fig. 2).

As is well known, the waveguide conductance G increases with the geometrical waveguide core area A and decreases with the length L of the CLIPP according to the relation

$$G = \sigma \frac{A}{L} \tag{a1}$$

where the electrical conductivity

$$\sigma = q\left(\mu_e N_e + \mu_h N_h\right) \tag{a2}$$

of the material depends on the electric charge q, on the mobility of electrons (μ_e) and holes (μ_h), and on the volume density of electrons (N_e) and holes (N_h). Since A and L are fixed by the waveguide geometry, the measured ΔG is essentially due to a conductivity variation $\Delta\sigma$, that is to either a variation in the mobility ($\Delta\mu$) and/or in the density (ΔN) of electrons and holes.

Here, we first demonstrate quantitatively that a variation $\Delta\mu$ in the carrier mobility does not explain the measured $\Delta\sigma$. Then, focusing on carrier density variation ΔN, we also rule out the existence of significant photocarrier generation mediated by two-photon absorption (TPA) effects, proving that surface state absorption (SSA) is the only candidate to be responsible for the observed changes in the waveguide conductance.

Variations of carrier mobility ($\Delta\mu$). In silicon optical waveguides carrier mobility can change because of (a) radiation pressure and electrostriction induced optical forces, (b) temperature, and (c) carrier density variations.

(a) Radiation pressure and electrostriction induced optical forces. From the measured ΔG versus P (see Fig. 2) we infer the value of $\Delta\mu$ that would be required to justify the observed change in the waveguide conductance. By substituting Eq. (a2) in Eq. (a1) and assuming that in p-doped silicon the conductivity is essentially due to free holes ($N_h = 10^{15}$ cm^{-3}, for commercial SOI wafers), we obtain the variation of mobility

$$\Delta\mu = \frac{\Delta\sigma}{qN_h} = \frac{1}{qN_h}\frac{L}{A}\Delta G \tag{a3}$$

shown in Fig. 7 for the same optical power range of Fig. 2. As an example, when the 480 nm wide waveguide operates at $P = 0$ dBm, we calculate $\Delta\mu = 417$ cm^2/(V·s), corresponding to a change in the relative hole mobility of $\Delta\mu/\mu_h = 0.93$. Such mobility variation would require the presence of a pressure on the waveguide of about 10^7–10^8 Pa [37] that is five orders of magnitude higher than the typical radiation pressure generated in the same optical power range of Fig. 2 [38]. Therefore, radiation pressure induced forces are ruled out as the physical effect responsible for the observed photocarrier generation. Likewise, also electrostriction is excluded, because it induces optical forces of about the same order of magnitude as radiation pressure [39].

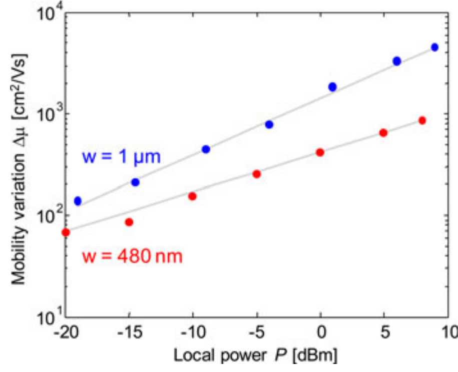

Fig. 7. Variation of the carrier mobility as a function of the local optical power for waveguides width of 480 nm (red circles) and 1 μm (blue circles); the grey solid line provides a linear fit of the experimental points.

(b) Temperature variations. The change of the waveguide conductance ΔG versus the waveguide temperature was measured in absence of light by controlling the chip temperature through a thermo-optic cooler placed below the sample. We found that a temperature change of 1 °C is responsible for $\Delta G = 1.17$ nS, this implying that a temperature variation by tens of degrees would be required to justify the results of Fig. 2. As the typical wavelength shift of the waveguide transmission spectrum amounts to 70 pm/°C [40], a considerable wavelength shift should be noticed. However, no significant wavelength shifts (>1 pm) were detected for the optical power range employed in the CLIPP measurement, thus excluding temperature variations as the responsible physical effect.

(c) Carrier density variations. In principle, a variation in the density of carriers induces a change in their mobility [41], [42]. At the typical doping level of 10^{15} cm^{-3} for SOI wafers, to halve the carrier mobility it is necessary to increase their density by at least two orders of magnitude [41], [42]. However, in the experiment of Fig. 2, we measured a photocarrier generation of the same order of magnitude as the typical doping level of the waveguide, and thus not sufficient to significantly modify the mobility.

Variations of carrier density (ΔN). In conventional silicon waveguides, free carrier density changes in presence of TPA and SSA. Photocarrier generation by TPA increases quadratically with the local optical power P [43]

$$\Delta N = \frac{\tau_{\text{eff}} \beta_{TPA}}{2h\nu} \frac{P^2}{A_{\text{eff}}^2} \tag{a4}$$

where τ_{eff} is the carrier recombination time, β_{TPA} is the TPA coefficient, $h\nu$ is the photon energy and A_{eff} the waveguide effective area. Since ΔG increases linearly with ΔN [see Eqs. (a1)–(a2)], TPA would require a quadratic relation between ΔG and P. Since in Fig. 2 such quadratic dependence is not observed, we rule out TPA as the physical mechanism responsible for the measured photocarrier generation.

In conclusion, SSA is the only physical effect that justifies quantitatively and qualitatively the behavior of the CLIPP.

Acknowledgment

The authors thank A. Canciamilla for the support in the design of the photonic circuits, D. Bianchi for discussions on the electronic instrumentation design, and the J. Watt Nanofabrication Centre (JWNC) staff at Glasgow University for the fabrication of the devices.

References

[1] T. Baehr-Jones, T. Pinguet, P. L. Guo-Quiang, S. Danziger, D. Prather, and M. Hochberg, “Myths and rumours of silicon photonics,” *Nat. Photon.*, vol. 6, no. 4, pp. 206–208, Apr. 2012.

[2] J. Sun, E. Timurdogan, A. Yaacobi, E. S. Hosseini, and M. R. Watts, “Large-scale nanophotonic phased array,” *Nature*, vol. 493, no. 7431, pp. 195–199, Jan. 2013.

[3] W. A. Zortman, D. C. Trotter, and M. R. Watts, “Silicon photonics manufacturing,” *Opt. Exp.*, vol. 18, no. 23, pp. 23598–23607, Oct. 2010.

[4] K. Padmaraju and K. Bergman, “Resolving the thermal challenges for silicon microring resonator devices,” *Nanophotonics*, vol. 2, pp. 1–14, Sep. 2013.

[5] J. Michel, J. Liu, and L. C. Kimerling, “High-performance Ge-on-Si photodetectors,” *Nat. Photon.*, vol. 4, no. 8, pp. 527–534, Aug. 2010.

[6] S. Assefa, F. Xia, and Y. Vlasov, “Reinventing germanium avalanche photodetector for nanophotonic on-chip optical interconnects,” *Nature*, vol. 464, no. 7285, pp. 80–84, Mar. 2010.

[7] J. K. Doylend and A. P. Knights, “The evolution of silicon photonics as an enabling technology for optical interconnection,” *Laser Photon. Rev.*, vol. 6, no. 4, pp. 504–525, Jul. 2012.

[8] T. K. Liang, H. K. Tsang, I. E. Day, J. Drake, and A. P. Knights, “Silicon waveguide two-photon absorption detector at 1.5 μm wavelength for autocorrelation measurements,” *Appl. Phys. Lett.*, vol. 81, no. 7, pp. 1323–1325, Aug. 2002.

[9] T. Tanabe, H. Sumikura, H. Taniyama, A. Shinya, and M. Notomi, “All-silicon sub-Gb/s telecom detector with low dark current and high quantum efficiency on chip,” *Appl. Phys. Lett.*, vol. 96, no. 10, pp. 101103–101113, Mar. 2010.

[10] T. Baehr-Jones, M. Hochberg, and A. Scherer, “Photodetection in silicon beyond the band edge with surface states,” *Opt. Exp.*, vol. 16, no. 3, pp. 1659–1668, Jan. 2008.

[11] H. Chen, X. Luo, and A. W. Poon, “Cavity-enhanced photocurrent generation by 1.55 μm wavelengths linear absorption in a p-i-n diode embedded silicon microring resonator,” *Appl. Phys. Lett.*, vol. 95, no. 17, pp. 171111–171113, Oct. 2009.

[12] J. D. B. Bradley, P. E. Jessop, and A. P. Knights, “Silicon waveguide-integrated optical power monitor with enhanced sensitivity at 1550 nm,” *Appl. Phys. Lett.*, vol. 86, no. 24, pp. 241103–241113, Jun. 2005.

[13] M. W. Geis, S. J. Spector, M. E. Grein, R. T. Schulein, J. U. Yoon, D. M. Lennon, S. Deneault, F. Gan, F. X. Kaertner, and T. M. Lyszczarz, “CMOS-compatible all-Si high-speed waveguide photodiodes with high responsivity in near-infrared communication band,” *Photon. Technol. Lett.*, vol. 19, no. 3, pp. 152–154, Feb. 2007.

[14] E. H. Nicollian and J. R. Brews, *MOS Physics and Technology*. New York, NY, USA: Wiley, 1982.

[15] W. Monch, *Semiconductor Surfaces and Interfaces*. Berlin, Germany: Springer-Verlag, 2001.

[16] M. Carminati, G. Ferrari, F. Guagliardo, and M. Sampietro, “ZeptoFarad capacitance detection with a miniaturized CMOS current front-end for nanoscale sensors,” *Sens. Actuators A, Phys.*, vol. 172, no. 1, pp. 117–123, Dec. 2011.

[17] M. Gnan, S. Thoms, D. S. Macintyre, R. M. De La Rue, and M. Sorel, “Fabrication of low-loss photonic wires in silicon-on-insulator using hydrogen silsesquioxane electron-beam resist,” *Electr. Lett.*, vol. 44, no. 2, pp. 115–116, Jan. 2008.

[18] F. Morichetti, A. Canciamilla, C. Ferrari, A. Samarelli, M. Sorel, and A. Melloni, “Travelling-wave resonant four-wave mixing breaks the limits of cavity-enhanced all-optical wavelength conversion,” *Nat. Commun.*, vol. 2, no. 296, May 2011.

[19] M. Casalino, G. Coppola, M. Iodice, I. Rendina, and L. Sirleto, “Near infrared sub-bandgap all-silicon photodetectors: State of the art and perspectives,” *Sensors*, vol. 10, no. 12, pp. 10571–10600, Nov. 2010.

[20] F. Morichetti, A. Canciamilla, C. Ferrari, M. Torregiani, A. Melloni, and M. Martinelli, “Roughness induced backscattering in optical silicon waveguides,” *Phys. Rev. Lett.*, vol. 104, no. 3, pp. 033902–033904, Jan. 2010.

[21] D. M. Kim, H. C. Kim, and H. T. Kim, “Photonic high-frequency capacitance-voltage characterization of interface states in metal-oxide-semiconductor capacitors,” *IEEE Trans. Electron. Devices*, vol. 49, no. 3, pp. 526–528, Mar. 2002.

[22] R. H. Bube, *Photoconductivity of Solids*. New York, NY, USA: Krieger, 1978.

[23] A. Goossens and J. Schoonman, “The impedance of surface recombination at illuminated semiconductor electrodes: A non-equilibrium approach,” *J. Electroanal. Chem.*, vol. 289, no. 1–2, pp. 11–27, Aug. 1990.

[24] J. R. Hauser, “Extraction of experimental mobility data for MOS devices,” *IEEE Trans. Electron. Devices*, vol. 43, no. 11, pp. 1981–1988, Nov. 1996.

[25] Q. Xu, B. Schmidt, A. Pradhan, and M. Lipson, “Micrometre-scale silicon electro-optic modulator,” *Nature*, vol. 435, no. 7040, pp. 325–327, May 2005.

[26] A. Griffith, J. Cardenas, C. B. Poitras, and M. Lipson, “High quality factor and high confinement silicon resonators using etchless process,” *Opt. Exp.*, vol. 20, no. 19, pp. 21341–21345, Sep. 2012.

[27] G. Cocorullo, F. G. Della Corte, and I. Rendina, “Temperature dependence of the thermo-optic coefficient in crystalline silicon between room temperature and 550 K at the wavelength of 1523 nm,” *Appl. Phys. Lett.*, vol. 74, no. 22, pp. 3338–33440, May 1999.

[28] R. S. Jacobsen, K. N. Andersen, P. I. Borel, J. Fage-Pedersen, L. H. Frandsen, O. Hansen, M. Kristensen, A. V. Lavrinenko, G. Moulin, H. Ou, C. Peucheret, B. Zsigri, and A. Bjarklev, “Strained silicon as a new electro-optic material,” *Nature*, vol. 441, no. 7090, pp. 199–200, May 2006.

[29] A. Manickam, A. Chevalier, M. McDermott, A. D. Ellington, and A. Hassibi, “A CMOS electrochemical impedance spectroscopy (EIS) biosensor array,” *IEEE Tran. Biomed. Circuits Syst.*, vol. 4, no. 6, pp. 379–390, Dec. 2010.

[30] C. R. Doerr, “Proposed architecture for MIMO optical demultiplexing using photonic integration,” *IEEE Photon. Technol. Lett.*, vol. 23, no. 21, pp. 1573–1575, Nov. 2011.

[31] N. Binkert, A. Davis, N. Jouppi, M. McLaren, N. Muralimanohar, R. Schreiber, and J. H. Ahn, “Optical high radix switch design,” *IEEE Micro Mag.*, vol. 32, no. 3, pp. 100–109, May/Jun. 2012.

[32] M. S. Luchansky and R. C. Bailey, “Rapid, multiparameter profiling of cellular secretion using silicon photonic microring resonator arrays,” *J. Amer. Chem. Soc.*, vol. 133, no. 50, pp. 20500–20506, Oct. 2011.

[33] J. L. O’Brien, “Optical quantum computing,” *Science*, vol. 318, no. 5856, pp. 1567–1570, Dec. 2007.

[34] P. J. Shadbolt, M. R. Verde, A. Peruzzo, A. Politi, A. Laing, M. Lobino, J. C. F. Matthews, M. G. Thompson, and J. L. O’Brien, “Generating, manipulating and measuring entanglement and mixture with a reconfigurable photonic circuit,” *Nat. Photon.*, vol. 6, no. 1, pp. 45–48, Jan. 2012.

[35] A. M. Broome, A. Fedrizzi, S. Rahimi-Keshari, J. Dove, S. Aaronson, T. C. Ralph, and A. G. White, “Photonic boson sampling in a tunable circuit,” *Science*, vol. 339, no. 6121, pp. 794–798, Feb. 2013.

[36] X. Cai, J. Wang, M. J. Strain, B. Johnson-Morris, J. Zhu, M. Sorel, J. L. O’Brien, M. G. Thompson, and S. Yu, “Integrated compact optical vortex beam emitters,” *Science*, vol. 338, no. 6105, pp. 363–366, Oct. 2012.

[37] R. He and P. Yang, “Giant piezoresistance effect in silicon nanowires,” *Nat. Nano.*, vol. 1, no. 1, pp. 42–46, Oct. 2006.

[38] P. T. Rakich, Z. Wang, and P. Davids, “Scaling of optical forces in dielectric waveguides: Rigorous connection between radiation pressure and dispersion,” *Opt. Lett.*, vol. 36, no. 2, pp. 217–219, Jan. 2011.

[39] P. T. Rakich, P. Davids, and Z. Wang, “Tailoring optical forces in waveguides through radiation pressure and electrostrictive forces,” *Opt. Exp.*, vol. 18, no. 14, pp. 14439–14453, Jun. 2010.

[40] S. Grillanda, V. Raghunathan, V. Singh, F. Morichetti, J. Michel, L. Kimerling, A. Melloni, and A. Agarwal, “Post-fabrication trimming of athermal silicon waveguides,” *Opt. Lett.*, vol. 38, no. 24, pp. 5450–5453, 2013.

[41] W. R. Thurber, R. L. Mattis, Y. M. Liu, and J. J. Filliben, “Resistivity-dopant density relationship for phosphorus-doped silicon,” *J. Electrochem. Soc.*, vol. 127, no. 8, pp. 1807–1812, Apr. 1980.

[42] D. A. Antoniadis, A. G. Gonzalez, and R. W. Dutton, “Boron in near-intrinsic <100> and <111> silicon under inert and oxidizing ambient—Diffusion and segregation,” *J. Electrochem. Soc.*, vol. 125, no. 5, pp. 813–819, May 1978.

[43] Q. Lin, O. J. Painter, and G. P. Agrawal, “Nonlinear optical phenomena in silicon waveguides: Modeling and applications,” *Opt. Exp.*, vol. 15, no. 25, pp. 16604–16644, Nov. 2007.